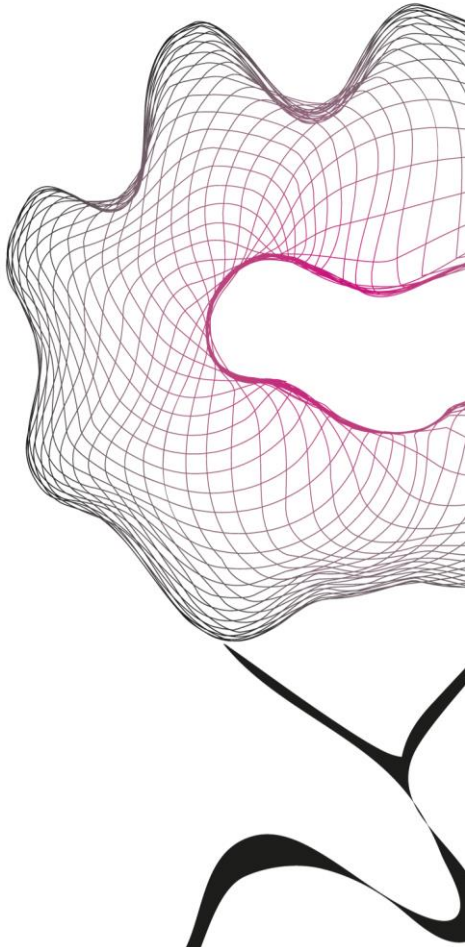


MASTER THESIS



CHARACTERIZATION OF THE BENDING STIFFNESS OF BULL SPERM FLAGELLUM USING MAGNETIC EXCITATION

Daniel Estima

FACULTY OF ENGINEERING TECHNOLOGY
DEPARTMENT OF BIOMECHANICAL ENGINEERING

EXAMINATION COMMITTEE
Prof. Sarthak Misra
Dr. Islam S. M. Khalil
Dr. Ir. A. Q. L. Keemink

DOCUMENT NUMBER
BE - 769

ABSTRACT

Magnetic systems can control microrobots for therapeutic purposes towards diseased sites, which holds substantial promise for drug delivery, cellular surgery and biosensing. Efficient motile function depends on coordinated interactions between active forces and passive mechanical resistance from the axonemal structure. However, on-demand precise control and details of coordination, including axonemal mechanics, remains unclear. We investigated the bending stiffness combining external magnetic actuation with a hybrid microrobot *IRONsperm*. This new wireless method expects to overcome the current hurdles in the sampling manoeuvring and data extraction, allowing more precise and accurate data estimation and increase of the amount of collected data in a shorter time interval. The estimated average flexural rigidity of immotile bull sperm cells coated with iron nanoparticles is equal to 2.1×10^{-8} N m with a standard deviation of 0.74×10^{-9} N m.

CONTENTS

- Abstract** **2**

- 1 Introduction** **4**

- 2 Background** **6**

- 3 Literature review** **8**
 - 3.1 Sperm ultrastructure 8
 - 3.2 Motion of Sperm Cells 9
 - 3.3 IRONSperm 12
 - 3.4 Bending Stiffness 15

- 4 Research design** **16**
 - 4.1 Magnetic Setup 16
 - 4.2 Experimental Setup 18
 - 4.2.1 Drag Coefficient Correction 19
 - 4.2.2 Bending Stiffness Estimation 21
 - 4.2.3 Data Acquisition 24

- 5 Results** **25**

- 6 Conclusions** **31**

- References** **32**

1 INTRODUCTION

Micro/nanorobotic systems capable of therapeutic action to diseased sites hold substantial promise for drug delivery, cellular surgery and biosensing. Advances in microrobotics have heightened the proficiency and scope of applications of these tiny robots.¹

Compared to conventional robots that rely on relatively large mechanical components, miniaturized robots appear to be more compelling for accurate transportation in complex and minuscule regions. The challenges in drug delivery include biocompatibility with the surrounding organic tissues and the path control on a cellular level.²

Thereupon, microrobots research has been growing as a promising platform for transporting targeted molecules or releasing payloads at predetermined confined destinations. Although on-demand precise control of the micro/nanorobot movement remains a major challenge.

To date, exceptional efforts have been dedicated to developing powerful wireless controlled microrobots for transportation and accurate targeted drug delivery systems. Recent developments have used acoustic propulsion methods to transport microscale objects, including the standing wave acoustic field,^{3,4} and surface acoustic wave.⁵ Both methods have exhibited great potential for the transport of micro-objects with high biocompatibility and precise control.

With a different approach, Guo J. *et al.* have employed strategically applied electric fields in 3D allowing high controllability of catalytic nanomotors.⁶ It has demonstrated new versatility in capturing, delivering, and loads release to designated placements. Similarly, magnetic fields have been used to control micro/nanorobots for payload transportation and drug delivery.⁷ Fig. 1.1 (e) shows artificial helical micropropellers, inspired by bacterial flagella (*e.g* Periplasmic flagella), driven by an external rotating magnetic field are an extremely effective solution for the propulsion of microrobots in water-like/Newtonian fluids.⁸

The use of flagella-like propellers has been recently added to a promising technique to allow bio-compatible microrobotic transport and targeting. Sperm and some eukaryote cells swim through flexible flagella that propagate bending waves at least ten times larger than bacterial flagella. The flexible filament (the tail) that can be actuated by the head allows propulsion in different viscous liquids. More specifically, a magnetic field precessing around the propulsion direction exerts a torque on the head, which combined with the fluid viscous drag induces a propagating transverse bending wave, as seen in Fig. 1.1 (d).^{7,11}

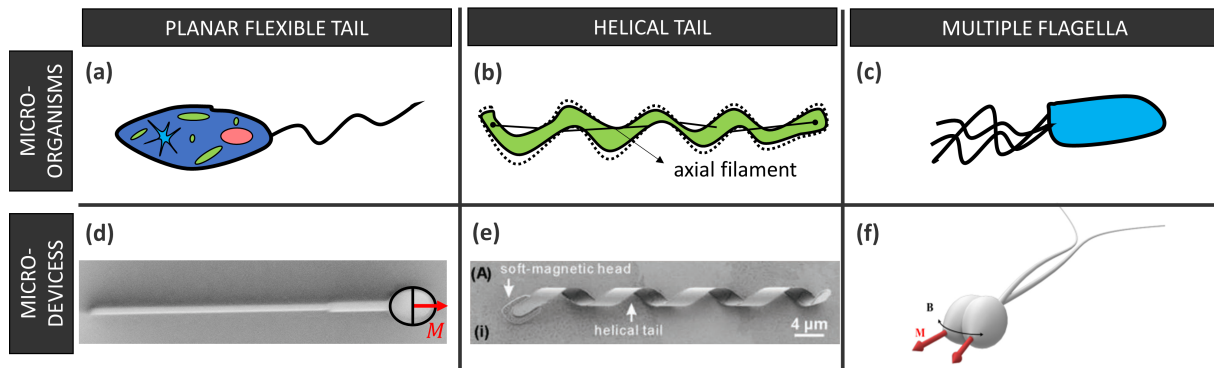


Figure 1.1: Illustration of bio-inspired magnetic swimming microrobots. (a) Single flexible flagella, e.g. Spirochaetes. (b) Rotating helical flagella around the axial filament, e.g. Periplasmic flagella. (c) Multiple flexible flagella, e.g. Lophotrichous. (d) MagnetoSperm: magnetic head and a flexible tail of 42 μm .⁹ (e) Helical robot with magnetized head and a diameter of 4 μm .⁸ (f) Theoretical model of a multi-flagella sperm cell with a magnetized head.¹⁰

Those magnetic applications mostly resemble biological systems, taking the Magnetotactic bacteria as an example, they are aquatic microorganisms with the ability to swim along the field lines of a magnetic field.¹² As a result, they have been the predominant viewpoint for the control of many microrobots using an external magnetic field.

Likewise, the use of hybrid flagellar microrobots can represent a new approach to the field of microrobotics. Biocompatibility is the main advantage over artificial propellers since it opens new doors for the development of a new generation of microrobots. Khalil *et al.*¹³ reported the possibility to propel immobile spermatozoa coated with magnetic iron nanoparticles, becoming the first bio-compatible microrobot passively controlled by an external magnetic field.

Any model of the behaviour of a controlled microrobot is dependant on a reliable estimate of the mechanical properties of the system. The study of the mechanical properties of the sperm flagella is essential to allow the control of the microrobot to follow the desired path. The bending stiffness is a fundamental material property and its determination is common in science and engineering. It is a key parameter in mechanical engineering design to predict the behaviour of the material under deformation forces or torques.

The flagella properties have been studied for over than 50 years and, with the evolution of the technology, the methods have been improving by giving more detailed information about the flagellar system with high accuracy. However, the current methodology is dependant on a manual torque appliance to the flagella and the direct contact with it, which represents a hard procedure to perform and time-demanding.

This paper proposes the first wireless and image-based methodology capable of accurately estimating the bending stiffness of flagellar systems. This new method expects to overcome the current hurdles in the sampling manoeuvring and data extraction, allowing more precise and accurate data estimation, increase of the amount of collected data in a shorter time interval.

2 BACKGROUND

Among various techniques available to date for wireless actuation of micro/nano-robots, the use of magnetic fields has been widely embraced due to their versatility and precision while controlling the locomotion of magnetic structures, and their excellent biocompatibility.¹⁴

Rémi Dreyfus *et al.* developed a linear chain of colloidal magnetic particles linked by DNA and attached to a red blood cell. The filament aligns with an external magnetic field and is actuated by oscillating a transverse field, acting as flexible artificial flagella.¹⁵ Several studies have been studying actuation on a magnetic head attached to flexible flagella by an alternating magnetic field.^{7, 16, 17}

Ghanbari *et al.* schemed magnetic actuation of artificial cilia using a variant field and showed the characteristic beating pattern of cilia, mimicking their natural counterparts.¹⁸ Recently, Khalil *et al.* has reported a magnetic microrobot that handles a planar wave of two soft flagella while swimming forward or backward.¹⁰

However, most of the current artificial microrobots are made with polymer basis and other non-bio-compatible materials. This remains itself a huge problem for the implementation of these tiny robots into a biological environment. Research of bio-compatible microrobots becomes essential for the future of drug delivery and biological swimmers. Consequently, this thesis will be focused primarily on the study and analysis of biocompatible robots. The use of spermatozoa has been recently recommended as peripherals of a microrobot because of their ability to carry drugs, strong flagellar driving source and, more importantly, full compatibility with biological systems.

Magnetotactic bacteria (MTB) represents the biological combination between flagellar propulsion and magnetic field actuation that was immediately the target of research to comprehend the motion and develop possibilities to turn it into a controllable microrobot.

Martel *et al.* shown that the manipulation of *Magnetospirillum gryphiswaldense* MTB is possible by modifying the torque on a chain of magnetosomes in the bacterium with a directional magnetic field.¹⁹ Lanauze *et al.* investigated a three-dimensional (3D) aggregation of MTB to allow a three degree-of-freedom (DOF) manipulation and guide the bacteria effectively in the human microvasculature to deliver a predefined dose of therapeutics.²⁰

On a different approach, resembling the design of eukaryotic protozoa, Benkoski *et al.* fabricated

artificial microscopic swimmers by assembling ferromagnetic cobalt nanoparticles and superparamagnetic magnetite colloids, which would form flagella-like assemblies, with a "head" + "tail" structure.²¹

Recently, a spermatozoa hybrid was developed and called IRONSperm, which consists of the assembly of magnetic nanoparticles with non-motile cells. The combination would rely on a partial coating of the sperm head with nanoparticles, which would enable propagation of a helical travelling wave along the flagella under the influence of a periodic magnetic field.¹³ Experiments successfully showed the ability to control the rate of progression of the bending waves throughout the passive flagella using the magnetic actuation field.

3 LITERATURE REVIEW

3.1 Sperm ultrastructure

To understand the flagellar events which are essential for the development of sperm motility, one must first consider the fundamental structure of the flagellum. Although there are species specific characteristics, mammalian spermatozoa share the same basic structure: head and a tail. The main function of the head is to deliver a set of DNA chromosomes to the oocyte. The function of the tail is to provide mobility to allow transport through the female reproductive tract. The flagellum can be differentiated in four regions: the head, the midpiece, the principal piece and the end piece.

The axoneme composition consists of two central microtubules connected by linkages surrounded by nine microtubule doublets.²² The doublet is composed by an A subunit forming a complete microtubule, and a B subunit (C-shaped) with its ends attached to the A subunit. In animals with internal fertilization, auxiliary dense fibres (outer dense fibres) and dibours sheath surround the axonemal structure. Attached to the A subunit are the dynein arms.

Dynein is an ATPase complex which translates chemical energy (ATP) into kinetic energy by allowing adjacent microtubules doublets to slide relative to each other, causing axonemal bending and hence movement.²³ This happens in an attachment-detachment cycle between the dynein arms and adjacent doublet. The adjacent doublets are connected by nexin links and it has been suggested that they allow regulation of the shear forces or assist in the retention of symmetry during doublet sliding.²⁴ Brokan *et al.* reported that nexin can be digested by elastase, causing an increase in the flagellar bend angle, and a decrease in flagellar beat frequency, suggesting that these links are involved in the regulation of the amplitude of ax-

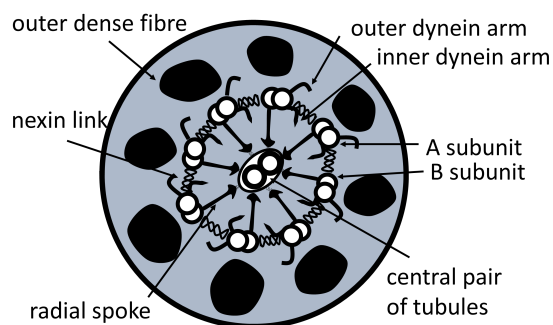


Figure 3.1: Transverse section of a mammalian sperm flagellum. The axoneme consists of nine outer subunit doublets surrounding a central pair of single microtubules. These beamlike components are interconnected by radial spokes and nexin-dynein regulatory complexes (N-DRC). Interdoublet sliding is driven by dynein motor proteins.

onemal bending.²⁵

The axoneme of a mammalian spermatozoon is surrounded by nine outer dense fibres. Each fibre is associated with a microtubule doublet. These fibres contain a cortex and medulla and are composed of a keratine-like protein.²⁶ The exact role of these fibres in sperm motility has not been determined conclusively.

The connecting piece is a short linking segment between the sperm head and flagellum. The midpiece of the mammalian spermatozoon goes from the distal end of the connecting piece to the annulus, an element marking the junction between the midpiece and the principal piece. It contains an arrangement of mitochondria that generates energy for flagellar movement.²⁷ The principal piece extends from the annulus to the terminal piece and is characterized by the presence of the fibrous sheath that has been hypothesized to support and restrict flagellar movement.²⁸

The terminal piece is the segment beyond the distal end of the fibrous sheath, where the axonemal elements terminate successfully, including the dynein arms disappearance and termination of the central pair of microtubules.^{29,30}

3.2 Motion of Sperm Cells

Over the past century, research of flagella movement focused on the natural movement of the flagellum towards the ovum. J. Gray presented the throughout the description of animal locomotion back in 1939.³¹ After several years, the undulatory propulsion became the focus of the investigation, starting to make breakthroughs over the factor of internal bending coupled with the lateral curvature and the magnitude of tangential thrust.³²

The spermatozoon tail movement can be described in terms of the form and speed of the bending waves which travel along the tail.³³ Flagellar beating comes from an asymmetric sliding of axonemal components, where the energy is converted to mechanical movement from ATP catalysis. With the proviso, propulsion forces of alive spermatozoon cells come from inner bending generation. Regardless of the power source, a propulsive force is generated by a corkscrew motion to create propulsion in low Reynolds numbers. As an example, Khalil *et al.*¹³ has shown the possibility to generate propulsion forces in immobile using an external source of energy. In either case, it is essential to analyse the motion of the sperm cells when a bending wave is generated, independently of the energy source feeding the system.

The propulsion of a spermatozoon depends on the fact that all the tangential forces acting along the body is compensated by propulsive components of forces acting normally to the surface of the body. Further, we shall consider forces exerted on a short element δs , shown in Fig. 3.2. The element's transverse velocity (V_y) depends on the form of the waves and their speed of propagation (V_ω). The transverse displacement has two components: (i) tangential displacement ($V_y \sin \theta$), and (ii) a normal displacement ($V_y \cos \theta$). Since the flagellum is emerged in

water, it offers resistance to movement and, consequently, this displacement results in reaction forces tangential and normal to the surface of the element.

As the element dimensions and the displacement speed are very low, the reaction forces can be approximated as directly proportional to the velocity of displacement and to the medium viscosity. Given that the tangential displacement is $V_y \sin \theta$, the tangential and normal drag can be written as $\xi_{\parallel} V_y \sin \theta$ and $\xi_{\perp} V_y \cos \theta$, respectively. Where ξ_{\parallel} and ξ_{\perp} are the resistance coefficients for a medium with known viscosity. Consequently, the forward thrust (δF_y) of propulsion is $(\xi_{\parallel} - \xi_{\perp}) V_y \cos \theta \sin \theta \delta s$.

If the spermatozoon is actively moving, each element is also moving along the axis of propulsion at a velocity (V_x). This is equivalent to a tangential displacement $V_x \cos \theta$ and a normal displacement $V_x \sin \theta$. The corresponding forces acting normally and tangentially are $\xi_{\parallel} V_x \sin \theta \delta s$ and $\xi_{\perp} V_x \cos \theta \delta s$. The total forces acting normally and tangentially to the surface coming from

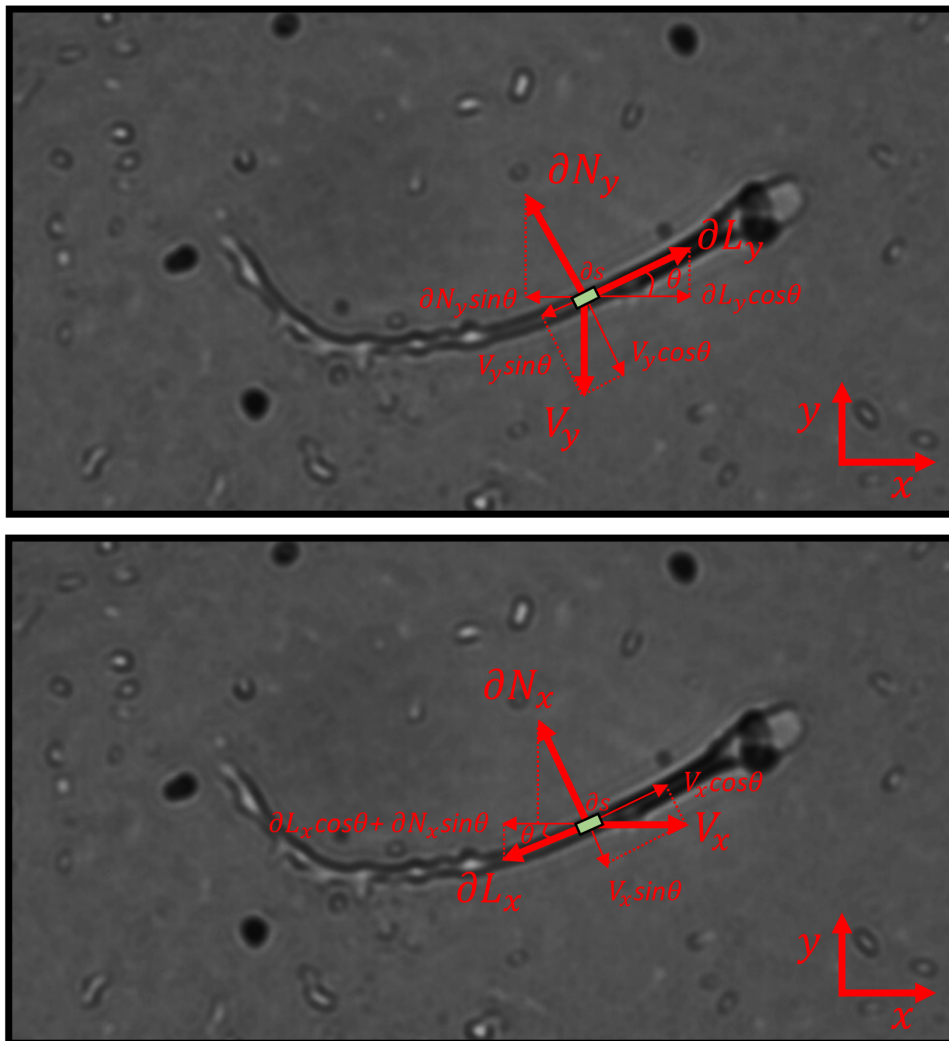


Figure 3.2: A. Diagram showing forces applied on a element δs when movement transversely across the axis of progression (x) at velocity V_y . B. Diagram showing forces applied on a element δs when displaced along x at velocity V_x .

the element's transverse and forward displacements:

$$\delta N = \xi_{||}(V_y \cos \theta - V_x \sin \theta)\delta s \quad (3.1)$$

$$\delta L = \xi_{\perp}(V_y \sin \theta + V_x \cos \theta)\delta s \quad (3.2)$$

The propulsive components of δN and δL along the axis of propulsion is $\delta N \sin \theta$ and $\delta L \cos \theta$, thus the resultant thrust force is:

$$\delta F = \delta N \sin \theta - \delta L \cos \theta = \frac{(\xi_{\perp} - \xi_{||})V_y \tan \theta - V_x(\xi_{||} + \xi_{\perp} \tan^2 \theta)}{1 + \tan^2 \theta} \delta s \quad (3.3)$$

Equation 3.3 can be re-written considering V_y as $\frac{\delta y}{\delta t}$ and the speed of propagation V_x as $f\lambda$, with f being the wave frequency and λ the wavelength. $\tan \theta$ can be approximated with $\frac{\delta y}{\delta x}$ assuming a small deformation of the flagellum.

$$\delta F = \frac{(\xi_{\perp} - \xi_{||})\frac{\delta y}{\delta t}\frac{\delta y}{\delta x} - f\lambda(\xi_{||} + \xi_{\perp}(\frac{\delta y}{\delta x})^2)}{1 + (\frac{\delta y}{\delta x})^2} \delta s \quad (3.4)$$

From Eq. 3.3, it is noted that the element can only exert a positive thrust force if $\xi_{||} > \xi_{\perp}$. Khalil *et al.* observed that motile cells generate greater force than magnetically actuated cells.¹³

However, the study of flagellar waveform does not depend only on the analysis of the force diagram of a moving flagellum. The bending waves are governed by the balance between the elastic and drag forces in low- Re (10^{-4}), where inertial forces are negligible, and the relation between the viscous force and velocity is linear over the beat cycle. Similarly, the bending waves actuated under an oscillating magnetic field have alike wave characteristics, with the difference that the wave propulsion comes from magnetic torque actuation.

In earlier studies of sperm movement, Rikmenspoel^{34,35} assumed the flagellum to be a thin rod along which the flexural vibrations propagate, as represented in Fig. 3.3. Their work reported that flagella waveform follows a helical motion along with the rotation of the cell around its longitudinal axis. Gray³³ studied the tail movement of sea urchin spermatozoa and found that the amplitude of the tail wave increased from the proximal towards the distal end of the tail. In both cases, the flagella movement analysis was accompanied by the scrutiny of the bending stiffness estimation (IE). Information about the bull or sea urchin flagella movement served to estimate IE and the accuracy of experimental results were justified by their proximity with the accepted limits for biological materials. In case of a small amplitude applied to the flagellum, the force balance governing equation approximates to:

$$IE \frac{\partial^4 U(x, t)}{\partial x^4} = -\varepsilon_{\perp} \frac{\partial U(x, t)}{\partial t} \quad (3.5)$$

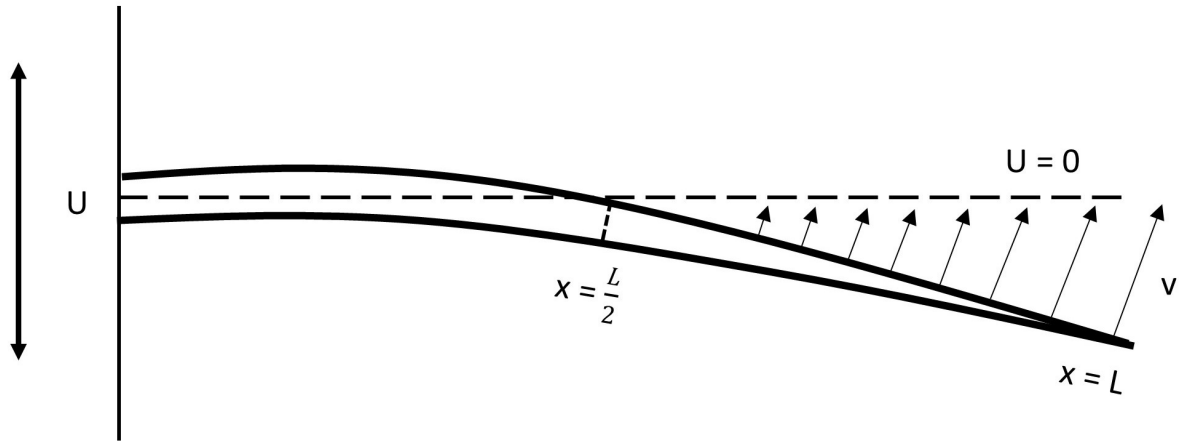


Figure 3.3: Diagram of the elastic model of the flagellum, showing the notation used. U represents the flagellar displacement from the equilibrium position ($U = 0$), the flagellum is assumed to be in equilibrium when completely straight. The base is at $x = z = 0$, the tip at $x = L$.

where $U(x,t)$ is the flagellar displacement along the flagellum length x , IE is the elastic rigidity or stiffness, t is time, x the coordinate along the length l of the flagellum, and ε_{\perp} is the effective drag coefficient. The force $IE \frac{\partial^4 U(x,t)}{\partial x^4}$ tends to restore the flagellum to its original natural shape, while $\varepsilon_{\perp} \frac{\partial U(x,t)}{\partial t}$ is the viscous drag force exerted by the surrounding fluid. Eq. 3.5 does not account for the bending moments that induce a travelling wave, independently of the power source e.g. ATP and magnetically actuated.

3.3 IRONSperm

The combination of bovine sperm cells and magnetic nanoparticles is a recent approach on the fashioning of flexible magnetic microrobots. The fabrication relies on the incubation of bovine non-motile sperm cells with magnetic nanoparticles. The electrostatic attraction between the nanoparticles (positively charged) and the sperm surface (negatively charged) empowers the genesis of biohybrid microrobots. The sperm cells provide the biological template, the coating of the nanoparticles allows the external magnetic actuation.

Magdanz *et al.*³⁶ has achieved forward propulsion by applying a precessing rotating magnetic field of low field strength (2–10 mT). With regards to the magnetic actuation, it revealed the non-uniform charge distribution of bovine sperm cells.³⁷ Consequently, coating along the cell would allow various segments to be individually magnetized that results in different magnetically actuated configurations (Fig. 3.4). Recalling Sec. 3.1, bovine spermatozoa is categorized by four morphological distinct areas: head, mid piece, principal piece and the distal end. Hence, the sperm-templated microrobots are categorized, depending on their particle attachment areas, into 15 groups (Fig. 3.4).

The total amount of attached nanoparticles is characterized by the net surface charge, whereas

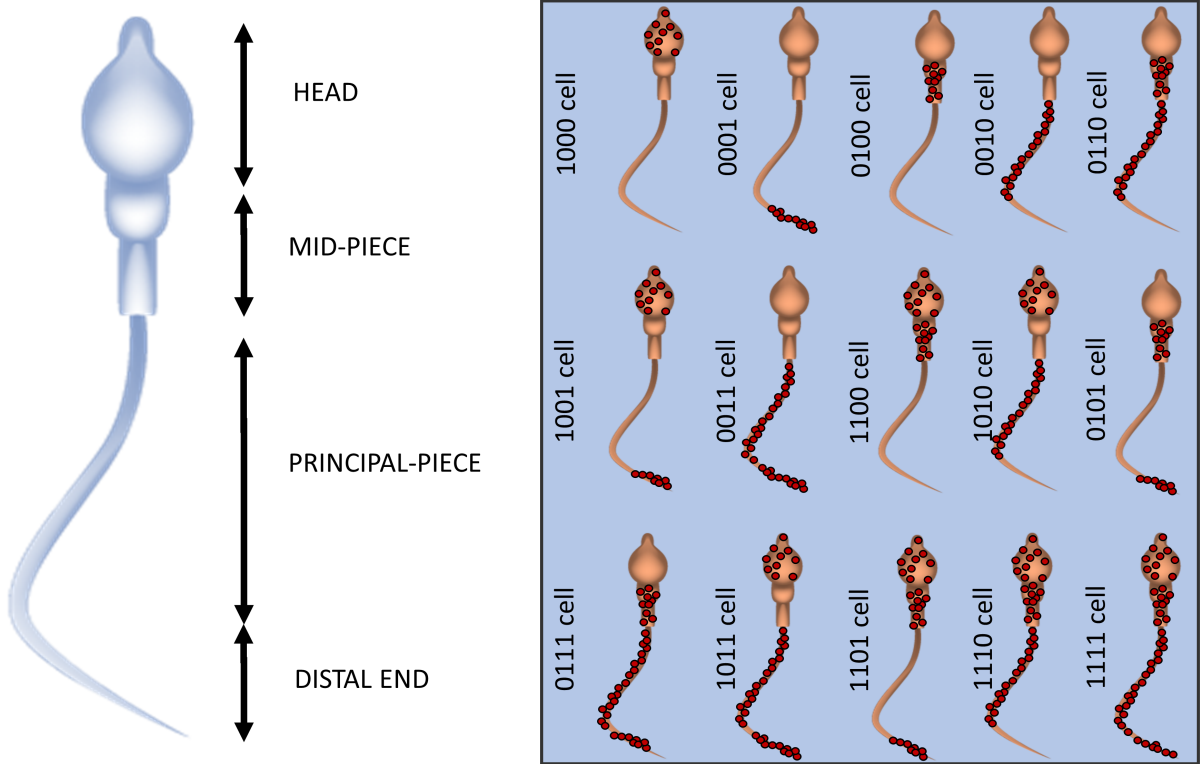


Figure 3.4: Bovine sperm cell consisting of a head 10 μm long, 5 μm wide and 1 μm flat, mid-piece 13 long μm , principal-piece 40 long μm and distal end 7 μm long. On the right all possible configurations of sperm-templated microrobots depending on attachment of magnetic nanoparticles to the different segments of bovine sperm cells.

the spatial distribution is dependant on the surrounding magnetic nanoparticles and the cell localized charge dispersion. The most common scenario takes place when the nanoparticles agglomerate and form clusters, resulting in a non-uniform of the magnetic coating along with the cell. A spare scenario happens when the coating is unwavering along with the cell (Group 1111) with particles uniformly distributed across all the four segments.

The application of an external magnetic field \mathbf{B} induces a magnetic moment that generates flagellar propulsion. The magnetic moment initiates transverse bending waves along the flagellum by magnetizing the clusters to a magnetization M_i , where i represents the cluster position on the segment head, mid-piece, principal piece, distal end. A cluster of magnetic particles will be considered a soft-magnetic body with a unique axis of symmetry resembling an ellipsoid.^{38,39}

The external magnetic field \mathbf{B} magnetizes the body to a magnetization \mathbf{M} . Now, to apply a magnetization model of a cluster of magnetic nanoparticles, we shall consider the linear-magnetization region, valid at low fields.⁴⁰ The magnetization of each cluster is dependant on the same field \mathbf{B} exerting a magnetic torque given by the following equation:

$$|T_i| = \frac{\nu_i |n_r - n_a|}{2n_a n_r \mu_0} |B|^2 \sin 2\theta \quad (3.6)$$

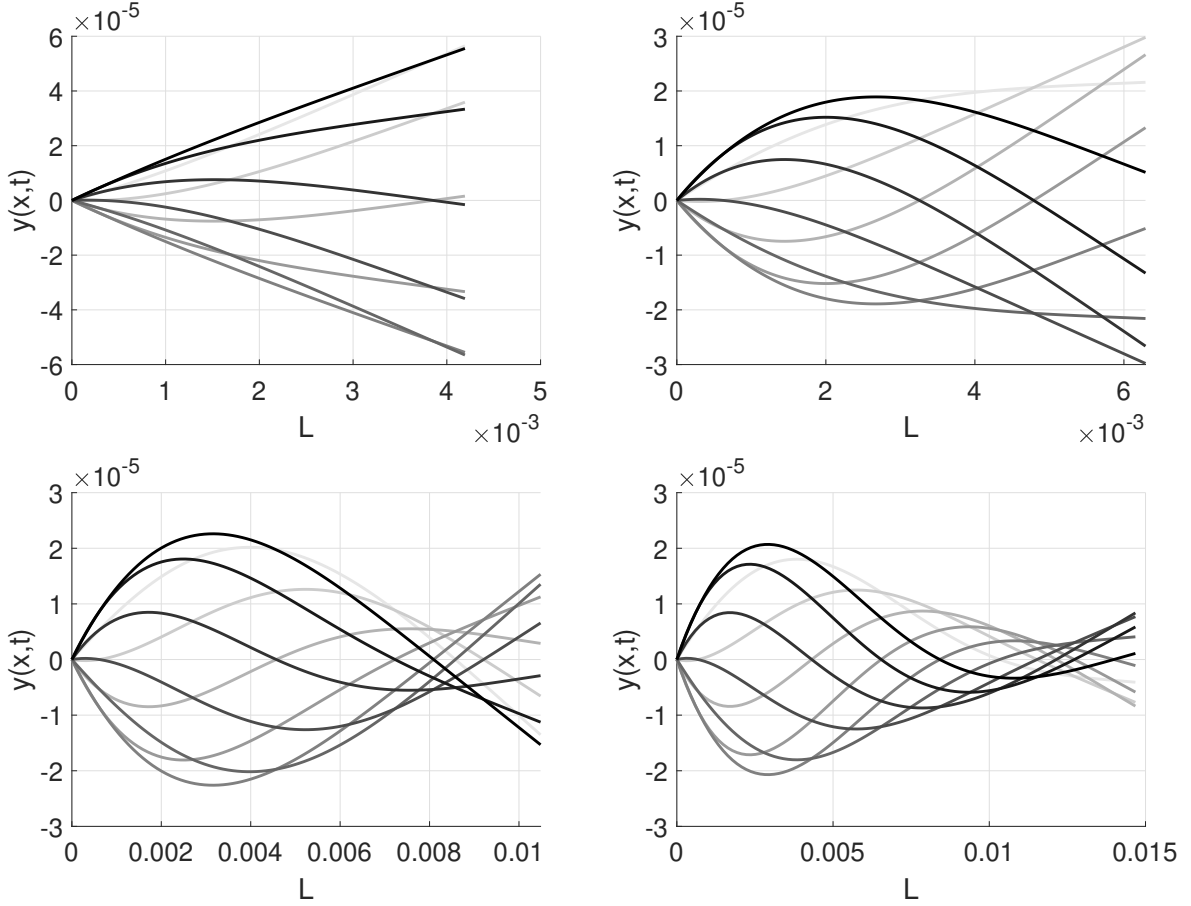


Figure 3.5: Illustration of various waveforms with different sperm number (Sp) values with $IE = 5 \times 10^{-20} \text{ N cm}^2$, $\omega = 1 \text{ Hz}$ and $\xi_{\perp} = 2.6 \times 10^{-3} \text{ N cm}^{-2} \text{ s}$. The tail length (L) is changing between graphs, having the following values: 100, 150, 250, 350, respectfully for the upper left and right, and bottom left and right.

where T_i is the magnetic torque exerted on the i th segment along the flagellum, ν_i is the magnetic material volume of the cluster. In addition, n_r and n_a are the demagnetization factors along the axis of symmetry and radial direction, respectively. μ_0 is the permeability of free space and θ is the angle between the local long-axis orientation and the external magnetic field.

As a result, the oscillation of the magnetic field leads to travelling waves along the cell allowing the microrobot to swim using flagellar propulsion. These bending moments induce a travelling wave producing a net thrust force, defined in Eq. 3.4, that propels the sperm cell forward. The generated waveform can assume different shapes, shown in Fig. 3.5, and it is dependant on different factors, such as the internal flagellar physical properties or the external drag resistance.

Recalling the sperm number definition

$$S_p = L \frac{IE^{\frac{1}{4}}}{\omega \xi_{\perp}} \quad (3.7)$$

ω is the rotation velocity directly related with external control. ξ_{\perp} is a known normal drag coefficient as well as L the sperm tail length. The flexibility (IE) remains solely unknown to allow wave

deformation prediction over time and, therefore, its inaccurate estimation remains a stumbling block in the control theory of flagellar microrobots.

3.4 Bending Stiffness

Bending stiffness estimation recalls a relevant applied physical basis regarding the vibration of flexible elements. Morse⁴¹ gives significant theoretical mathematical wave analysis that is currently essential for the investigation of wave movement analysis.

Machin⁴² showed a theoretical approach to study the wave propagation along an elastic filament in a viscous medium. Applying the following assumptions: the flagellum has a circular cross-section; the waves propagate in a plane; the filament immersed in a viscous fluid with density ρ and viscosity μ , characterized by low Reynolds number ($Re = \frac{\rho|V_r|L}{\mu}$) hydrodynamics in the order of $10^{-3} - 10^{-5}$, where L and V_r are the length and linear velocity of the filament in its reference frame, respectfully. By re-arranging Eq. 3.5, we get the following differential equation:

$$\frac{\partial^4 U(x, t)}{\partial x^4} = -\frac{1}{c^4} \frac{\partial U(x, t)}{\partial t} \quad (3.8)$$

With,

$$c = \sqrt[4]{\frac{IE}{\varepsilon_{\perp}}} \quad (3.9)$$

The steady solution of the differential equation is:

$$U(x, t) = e^{i2\pi ft} (Ae^{r_1 x/l_0} + Be^{r_2 x/l_0} + Ce^{r_3 x/l_0} + De^{r_4 x/l_0}) \quad (3.10)$$

With f being the frequency of oscillation, r_1, r_2, r_3, r_4 are the four differential solutions. A, B, C, D are complex constrains directly related with the boundary conditions imposed on the system. The boundary conditions have a significant impact in the computed waveform of the flagellum that depends from case to case, investigated throughout Marchin's work.⁴²

Rikmenspoel^{34, 35, 43} continued determining the sperm tail stiffness from the experimentally observed waveforms. An important consideration was taken by considering the sperm flagellum to be a tapered thin rod, which as also been corroborated by Omoto and Brokaw.⁴⁴ The flagellum was clamped at the head ($x = 0$) and the movement that was driving the rod was defined as

$$U(0, t) = a \sin \omega t \quad (3.11)$$

$$\frac{\partial U(0, t)}{\partial x} = b \cos \omega t \quad (3.12)$$

a, b, U were obtained experimentally. The experimental bending stiffness of motile urchin sperm flagellum was found ($\approx 6 \times 10^{-11} \text{ N}\mu\text{m}^2$). Later on, the same theoretical implementation was performed in active Cilia and showed that the bending stiffness decreased with the swimming frequency.⁴⁵ All of these works show the importance of the boundary conditions in the estimation of the bending stiffness.

4 RESEARCH DESIGN

4.1 Magnetic Setup

The magnetic actuation is an essential part of the control of the IRONSperm. The grounded Helmholtz three coil configuration successfully applied a 3D magnetic actuation in this micro-robots. The problem using that configuration is that the Helmholtz holds a closed and small workspace that cannot fit in the Zeiss Axio A6 inverted microscope. This microscope has a gentle LED illumination that allows high-resolution imaging of biological samples. From this problem, we had to build a new setup for the magnetic actuation.

The design of the coil began with a few fundamental goals as follows:

- Has our goal is to study the planar movement of the sperm cells, the first design choice consisted of the creating of a magnetic field tangent to the sample probe.
- To avoid the same problem with the Helmholtz setup, the magnetic setup should be portable and easily removable from the microscope platform.
- Soft-magnetic cores were chosen over air cores because they create a field approximately 20 times stronger. However, the generated magnetic field needs to be constrained within the linear magnetization region to allow the linear superimposition of their individual fields.¹⁴
- The workspace should be able to generate sufficient magnetic forces in any direction of the planar field of the samples.

The methodology to reach this setup started by analysing the magnetic field direction in space. Using Matlab, the first analysis simulated the 2D magnetic distribution for ideal solenoids, following the calculations of N. Derby.⁴⁶ Fig. 4.1 (a) shows the representation of the magnetic field generated by a cylindrical solenoid.

The study of the magnetic distribution of this model sets the first mark to verify the feasibility of the planar field appliance given a certain tilted angle of the magnetic coils. Furthermore, we will be able to scrutinize the coil position with respect to the sample position, maximizing the magnetic strength. This maximization has some constraints set by the microscope platform:

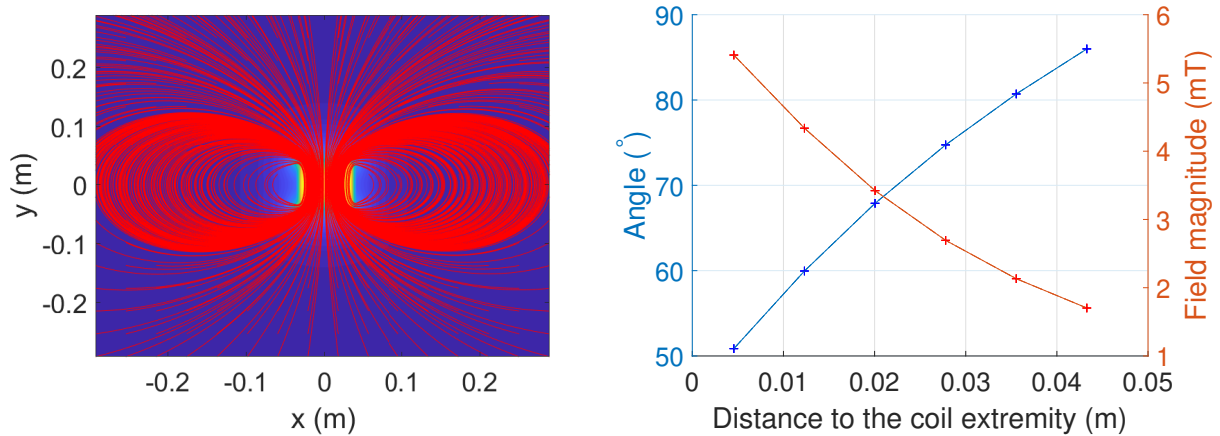


Figure 4.1: (a) Magnetic field generated by a solenoid. The red lines show the direction of the magnetic field. The color grading represents the magnetic amplitude. (b) The magnetic field angle profile along with the distance with respect to the coil rotating pivot point (blue line). The field magnitude related to the distance to the coil is illustrated in the red curve.

the magnetic coils cannot be above the sample plane since it would collide with the upper LED illumination, nor below the sample plane due to obstruction of the microscope base. Additionally, the coils cannot be closer than a radius of 2 cm to the sample position, as it would block the light from the upper LED and, once again, would collide with the illumination source.

From the spatial constraints described above, the following design choices held place.

The coil position would be as closest as possible to the sample hence maximizing the magnetic field. Besides, we shall find the inclination of the magnetic coil such that the magnetic field is tangent to the sample area.

Fig. 4.1 (b) illustrates the angle of the magnetic field with the long axis of the solenoid at a point of certain distance with the coil pivot point. The field magnitude profile also shows an exponential decrease with the distance to the coil extremity.

Through the use of a digital 3D teslameter, we experimentally determined the estimation of the correct inclination and the distance coil-sample to validate results from the model above described. By holding the teslameter static, the magnetic coil rotates around a pivot point 3 cm away from the teslameter measuring tip. Along with the rotation, the magnetic field direction was being measured and mapped. The coil inclination angle estimate happens when the vertical magnetic field is zero.

The mobility of the workspace comes from a setup resting in a sliding structure fitting above the microscope platform. Resulting in a stable fixed position but also easy to remove by sliding the structure laterally away from the microscopic base. Moreover, a tilted wedge, shown in Fig. 4.2 (5), was applied to act as a pivot point of rotation of the coils and preventing them from sliding along the microscopic table.

Also, a Plexiglas disk (shown on Fig. 4.2 (4)) replaced the metallic disk that belonged to the

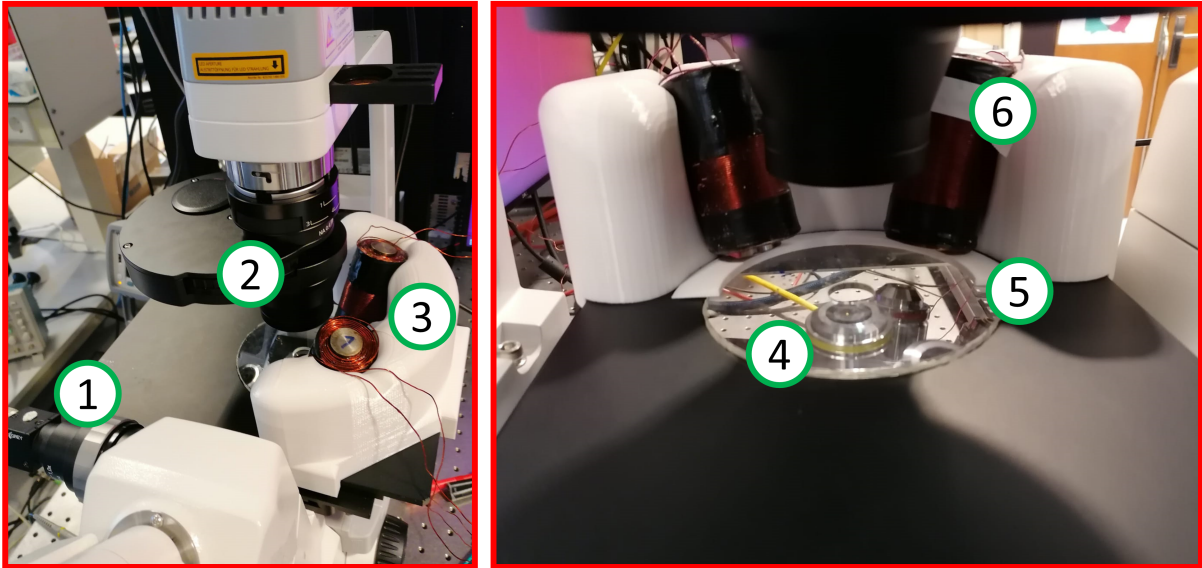


Figure 4.2: Illustration of the experimental setup to hold the magnetic coils. (1) Camera used to record the microscopic images. (2) Illumination LED and image filter (3) 3D printed piece to hold the magnetic coils and deliver a planar magnetic field on the sample position (4) Plexiglas disk to hold the sample lamina (5) Semi-circular wedge to support the coil position (6) Magnetic coil

microscope, which would interfere with the direction of the magnetic field. This material was chosen due to its strength to support the weight.

The magnetic field was provided using the dynamic Servo Drive EtherCAT and controlled using a self-made Qt GUI window. The Magnetically-Actuated System was designed as a 3D model in SolidWorks (Dassault Systèmes SolidWorks Corp., Waltham, Massachusetts, USA). A photo of the magnetic setup is shown in Fig. 4.2.

4.2 Experimental Setup

To facilitate sperm tracking, we made use of the fact that sperm cells become hydrodynamically trapped near a planar boundary surface⁴⁷ since they swim there with an approximately planar flagellar beat, allowing to simplify the analysis to two spatial dimensions.⁴⁸ This phenomenon happens in two boundary conditions, the air-liquid interface at the top of the sample medium and the glass-liquid interface at the bottom of the container. Ferraci *et al.*⁴⁹ proved that microorganisms swim in the water-air boundary without deforming the interface. Even though this phenomenon ensures a planar motion, ideal for microscopic imaging, the planar surface is highly influenced by the outside environment such as airflow and vibrations. Besides, the flagellar organism will be constantly floating freely, which disables any possibility to clamp the head or any other member of the flagellum.

The second phenomena, the glass-liquid interface at the container bottom, has the advan-

tage of repeatability because of the natural sedimentation of the IRONSperm at the bottom of the container. Khalil *et al.*¹³ has observed this tendency of sedimentation while analysing the IRONSperm swimming properties they had to compensate the gravity influence by making the robot swim upwards, counteracting the gravity movement. It has been also observed that the head very often got attached to the bottom glass, preventing the IRONSperm to swim upwards, which may be used in our favour from now on. Thus, our experimental analysis will rely on the sedimentation and attachment of the sperm's head with the bottom of the Petri dish.

4.2.1 Drag Coefficient Correction

The viscosity of the medium is highly important as it has been proven that is directly related to the flagellar beating movement. More specifically, D. J. Smith⁵⁰ has shown that progressing waves increase in curvature approximately linearly with the viscosity, except for a sharp increase over the principal/distal piece of the flagellum. Toru Hyakutake⁵¹ also reported that not only the increase of progressive thrust with the flagellar tip curvature but also motile sperm seem to move more efficiently in high shear-thinning viscoelastic fluids than that in Newtonian fluids. Consequently, the fluid viscosity needs to be approximately known during the experimental analysis.

Furthermore, the normal drag coefficient on any filament is clearly altered by the presence of any nearby boundary. The fact that our experiments will be nearby the bottom container is contingent upon changes on the magnitude of the normal drag coefficient ε_{\perp} . The influence of the surface plays an important role and can be described by the following equation⁵²

$$\varepsilon_{\perp} = \frac{4\pi\eta}{\log\left(\frac{2h}{r_t}\right) - 0.301} \quad (4.1)$$

where η is the viscosity of the fluid constant, r_t the cross-section radius of the tail and h is the distance between the flagella and the nearest surface

Fig. 4.3 reveals the growth of the drag coefficient with the proximity with the nearby surface, with a decrease of h magnitude. Recurrent cases do not need to take the nearby surface influence into account as a result of a distance higher than 20 μm , where the coefficient magnitude converges to a constant value. However, when studying sedimentary elements ($h \leq 10 \mu\text{m}$), the drag magnitude is significantly influenced and, consequently, shall be corrected accordingly. The sperm head can be approximated to a planar ellipsoid resembling shape with a bigger axis equal to $8.63(\pm 3.1)\mu\text{m}$ and smaller axis $4.34(\pm 3.6)\mu\text{m}$ ⁵³ and thickness $2(\pm 0.5)\mu\text{m}$ values that will be important for the drag coefficient estimation for next section.

The IRONSperm dynamic excitation will be applied in specific conditions to ensure that the sperm cell is being held in one certain place where the rotation will be applied. In conventional methods, the head is fixed manually with a micro-probe or a laser-tweezer. The goal of this fixation ensures that the moment applied to the tail is being applied only on the tale and does

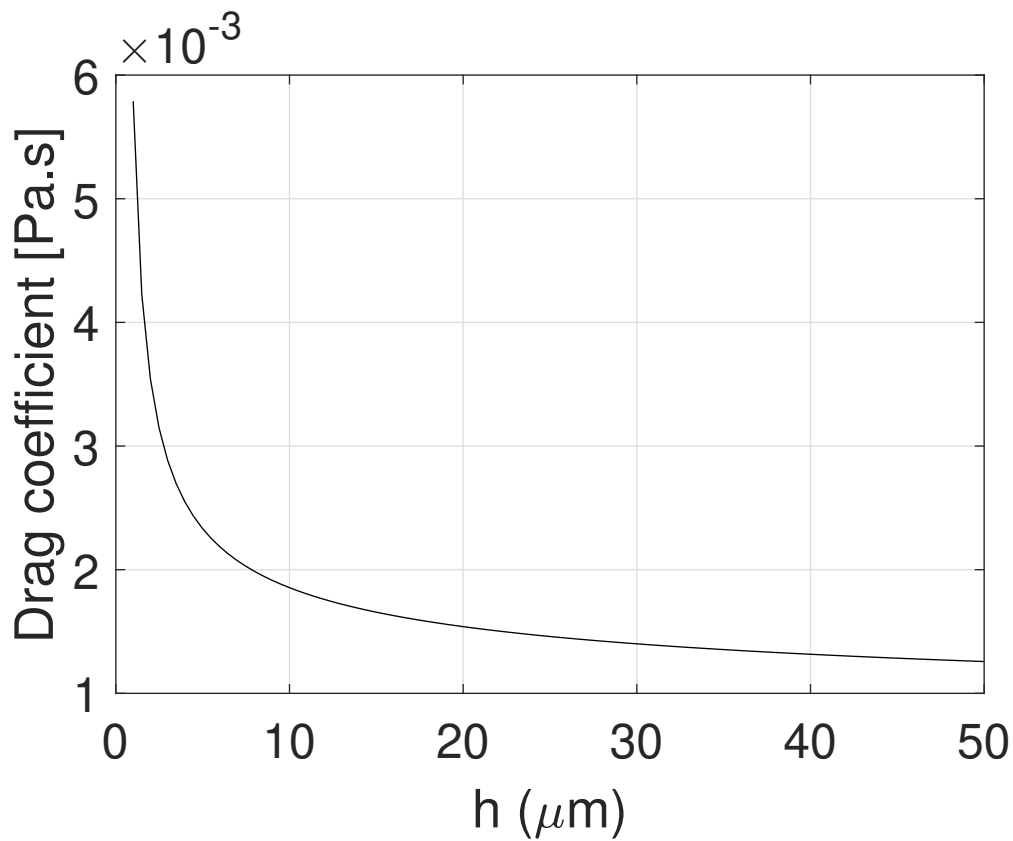


Figure 4.3: The influence of proximity to a nearby surface (h) on the normal drag coefficient ε_{\perp} calculated using 4.1. The coefficient is computed for a 60 μm -long IRONSperm with a tail radius of 0.5 μm and in a medium with viscosity of 0.95 Pa.s

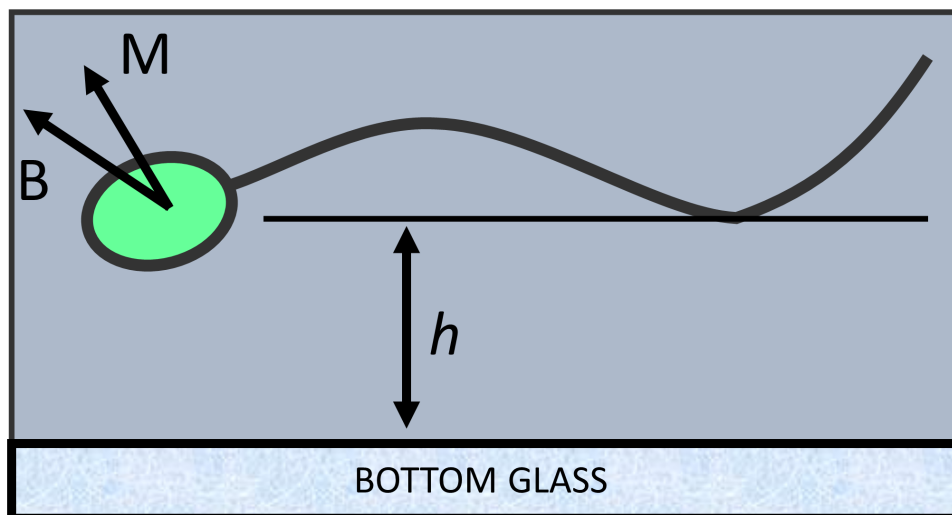


Figure 4.4: Illustration of the close boundary effect of the sperm's flagellum at a distance h from the bottom glass surface. The sperm cells is magnetically actuated at the head by an external magnetic field \mathbf{B} . \mathbf{M} is the resultant magnetizing force inside the material, differing from \mathbf{B} due to the demagnetization factor of any soft magnetic material.

not create any rotations of the entire flagellar system (head+flagellum). Consequently, it is highly important to find an effective way of ensuring a contactless constrain that ensures this fixation of the flagellum to a specific reference frame.

The solution implemented throughout our experimental study used the natural attachment of the sperm head to the bottom of the Petri dish in our favour. From that point of contact, the entire centre of rotation of the IRONSperm will be done around that fixed point also called as rotational constrain. The above-described methodology has been implemented in previous studies, such as the work of Lesich *et al.*^{54,55} where cells were allowed to precipitate and adhere by their head to the glass and only the ones with the flagellum free to beat would be analysed.

Once the cell gets to a stable impaled configuration, the experimenter shall tap the tabletop forcing the cell and probe to oscillate slightly. This was done to verify that the flagellum's head was successfully stuck to the bottom surface and the tail was free to move. Subsequently, an oscillating magnetic field is applied to check whether the pivot point does not oscillate with the variation of the magnetic field. In the case of rotation, the sperm is not considered for the experimental analysis.

4.2.2 Bending Stiffness Estimation

The most used form of computing the bending stiffness of any flagellar compound is by a manipulatory technique to impale the flagella and get statistical analysis of this motionless system.

Lindemann *et al.*⁵⁶ have been using a capillary micro-probe to impale and manipulate individual sperm. That was possible by holding the probe in a piezoelectric driver to allow a fast advance of the probe to successfully impale the sperm head.⁵⁵ Consequently, the bending stiffness is found using the probe tip to apply a flagellar displacement and utilising the force applied to the probe by the attached bead. The two methods used to apply the displacement are: to move the microscope laterally or to move the probe along its longitudinal axis and back to the original position.

The problem we shall tackle is the dependence in a microprobe instrument that demands proficient routine and technique manoeuvring the device, resulting in a time-consuming task. Given an external magnetic field \mathbf{B} , a torque is generated on the clusters scattered around the flagellum that aligns itself with the external magnetic direction. Hence, by controlling the external magnetic field direction, we can apply any displacement upon the IRONSperm flagellum.

Next, we will describe the two different approaches we applied to compute the bending stiffness in our experimental data.

Relaxation Methodology

The bending stiffness determination happens under the same condition described above, with the sperm head always anchored and, during relaxation, the distal end is free. The flagellum constitutes a rod of known length l . Eq. 3.5, the fourth-order partial differential equation, can be solved by applying the following boundary conditions:

$$U(0, t) = \frac{\partial U(0, t)}{\partial x} = \frac{\partial^2 U(l, t)}{\partial x^2} = \frac{\partial^3 U(l, t)}{\partial x^3} = 0 \quad (4.2)$$

For $x = l$ the end is free with the bending moment and shear force being equal to zero. The differential equation solution comes by replacing

$$U(x, t) = e^{-\frac{t}{\tau}} Z(x, 0) \quad (4.3)$$

The equation above describes the natural relaxation movement over time or, in other words, the elastic behaviour of the sperm flagellum tending to its equilibrium position. By replacing it, we obtain the following

$$\frac{d^4 Z(x)}{dx^4} = \lambda^4 \frac{dZ(x)}{dt} \quad (4.4)$$

where

$$\lambda^4 = \frac{\varepsilon_{\perp}}{IE\tau} \quad (4.5)$$

Hence there are four particular solutions of the differential equation for $Z(x)$:

$$e^{\lambda x}, e^{-\lambda x}, e^{i\lambda x}, e^{-i\lambda x} \quad (4.6)$$

which combining conveniently results in the following general solution:

$$Z(x) = A \sinh kx + B \cosh kx + C \sin kx + D \cos kx \quad (4.7)$$

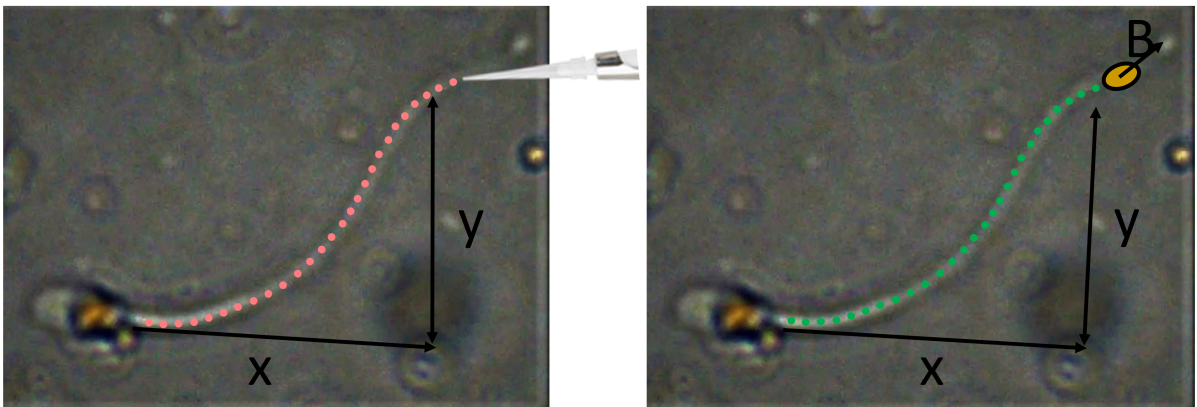


Figure 4.5: Left: Manually appliance of flagellar displacement using a micro-probe with a clamped head. Right: Magnetically and contactless methodology to generate flagellar displacement with an anchored head to the bottom of the container.

According to the boundary conditions (Eq. 4.2), there are four relations between the constants of integration A, B, C, D , from which we obtain through elimination the equation:

$$\cos \lambda l \cosh \lambda l = -1 \quad (4.8)$$

This equation yields an infinity of roots at intervals which asymptotically become

$$\lambda_i = \frac{\mu_i}{l} \quad (4.9)$$

$$\lambda_{n+1} - \lambda_n = \frac{\pi}{l} \quad (4.10)$$

The first node is equal to

$$\lambda_1 = \frac{1.875}{l} \quad (4.11)$$

Each of the nodes of the equation 4.10 has a correspondent decay time. The exponential decaying time constant depends on the mode number $n = 1, 2, 3, \dots$ and it is defined by combining Eqs. 4.5 and 4.9

$$\frac{1}{\tau_i} = \left(\frac{\mu_i}{l}\right)^4 \frac{IE}{\varepsilon_{\perp}} \quad (4.12)$$

The values ε_{\perp} and l are known. τ_i is experimentally measured decay time. In principle, any waveform can be identified by superposing multiple hydrodynamic modes found in the solution. Similar with the Fourier analysis, where any time-varying signal is expressed as the sum of cosine and sine modes, we may superpose the relaxation of the constituent modes to obtain the relaxation dynamics of any arbitrarily bent. In addition, the time constant Eq. 4.12 implies that as i increases, τ_i should decrease. In other words, the lower order modes relax more slowly than the higher-order modes and thus the first mode which relaxes the slowest. The lower order modes represent the flagellum of low stiffness and higher damping characteristic.

Lindemann C.⁵⁶ applied this equations and experimentally measuring relaxation times after manually applying a flagellar displacement using a micro-probe. The theory behind it has shown to successfully measure bending stiffness, being that the reason why it will be used throughout our experimental analysis.

Direct Methodology

The direct methodology represents a different approach solving the equation of motion to get the bending stiffness estimate. Disregarding the necessity to resolve the differential equation, we apply directly the information taken from the shape and velocity. The analysis can be divided in four major steps. First, we characterize and subtract the gross motion of the cell body so that the flagellar motion can be described with respect to a fixed reference frame with its origin at the proximal end of the flagellum. Second, we convert the Cartesian (x,y) coordinates from

pixel to μm , with respect to the equilibrium waveform, generating a 2D flagellum-shaped "cloud" of points, from each video image. After, the clouds of points are fit to a smooth, time-periodic surface of shear displacement as a function of time and space.

From the fitted data, we can now apply the equation of motion of a flagellar system

$$IE \frac{\partial^4 U(x, t)}{\partial x^4} = -\varepsilon_{\perp} \frac{\partial U(x, t)}{\partial t} \quad (4.13)$$

Where IE represents the bending stiffness, the current unknown value, ε_{\perp} is the normal drag and is directly related to the flagellum velocity.

From the experimental data we can extract $\frac{\partial^4 U(x, t)}{\partial x^4}$ and $\frac{\partial U(x, t)}{\partial t}$. In 4.13, IE is solved such that the following objective function is minimized:

$$\min_{IE} \xi = \left\| IE \frac{\partial^4 U(x, t)}{\partial x^4} + \varepsilon_{\perp} \frac{\partial U(x, t)}{\partial t} \right\|^2 \quad (4.14)$$

Applying both measurements in the equation above, we can get an estimation of the bending stiffness. This optimization routine is solved iteratively using nonlinear optimization using Matlab, and a polynomial fitting performed smoothing of the measured flagellar waveform.

4.2.3 Data Acquisition

The data were acquired using the Zeiss Axio Vert.A1 microscope using the software ZEN 2.6 lite to record the videos and change the specifications, such as frame rate and resolution. The videos were acquired at 30 frames per second, with a 50x objective and an imaging filter. Frame-by-frame waveform analysis was done using Matlab software. The change in deviation of the flagellum from the equilibrium position was measured as the flagellum returned to its equilibrium state.

The data collection was done following the next steps

- Converting the video into a sequence of .JPG images and manually assigning 40 points along the arc length of the spermatozoon's flagellum, as shown in the Fig. 5.1
- Fitting the waveform to a spatial polynomial of 4th order (higher-order polynomials did not show any significant improvement on the curve fitting error)
- Fitting the spatial coefficient time-evolution to a time-variant polynomial. This was done to recompose the time discontinuities between frames
- The time derivative ($\frac{\partial U(x, t)}{\partial t}$), 4th spatial derivative ($\frac{\partial^4 U(x, t)}{\partial x^4}$) and relaxation time (τ) were extracted from the experimental data

5 RESULTS

The time-course of the displacement of the flagella while relaxing towards the equilibrium position was plotted in Fig. 5.1. The first point used in plotting $[U(x, 0)]$ was always taken one or more frames after the release of the flagellum from the probe. This insured that the flagellum was already in the process of relaxing at time zero. For each sperm cell tried, a total of 10 trials were done at the same displacement made. In addition, for the same sperm cell, different displacements were applied to check the variation of it between different relaxation times.

The data-points were fitted to a polynomial of 4th order giving a root-mean-square deviation

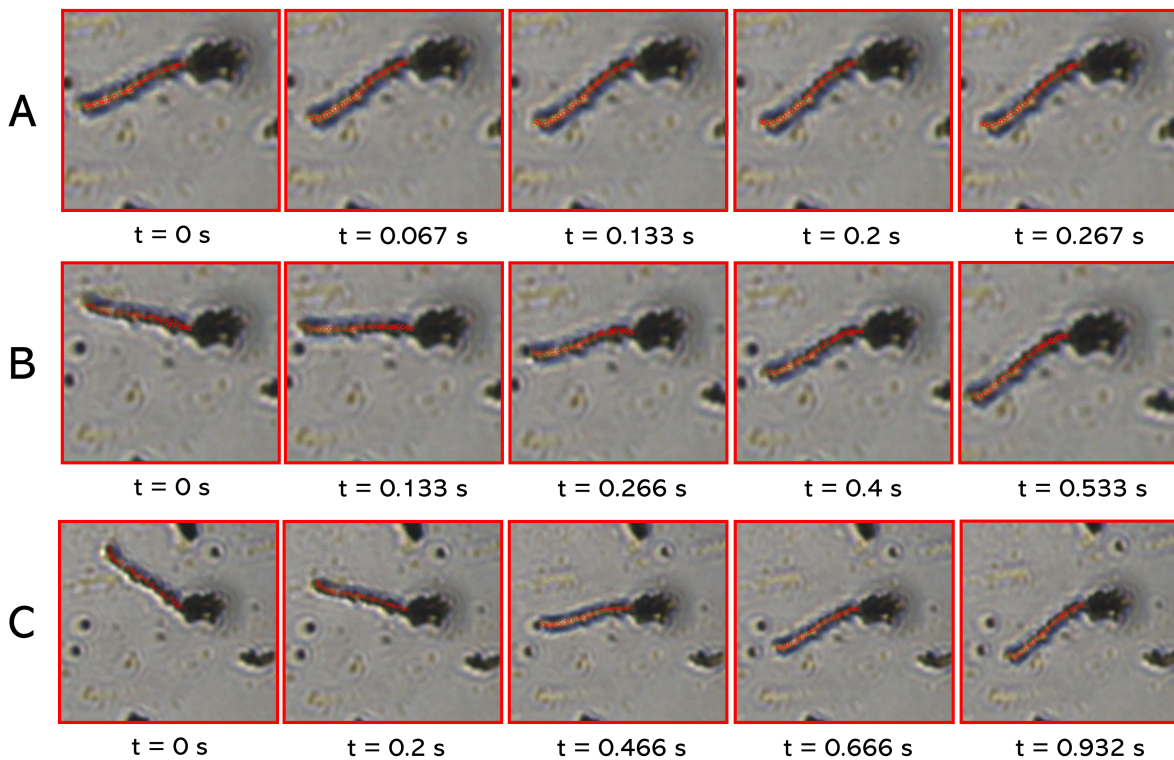


Figure 5.1: Flagellum relaxation over time. The flagellum relaxation is shown from left to right. The left frame shows the flagellum waveform right after the release of the magnetic field, that is $t = 0$. The last frame on the right shows the flagellum waveform at the equilibrium state. For this experiment, the flagellum took 0.267 s to return to its equilibrium state. (A) represents a small flagellar displacement ($4.24(92) \mu\text{m}$). (B) represents a flagellar displacement of $15.16(75) \mu\text{m}$. (C) represents a flagellar displacement of $22.84(52) \mu\text{m}$

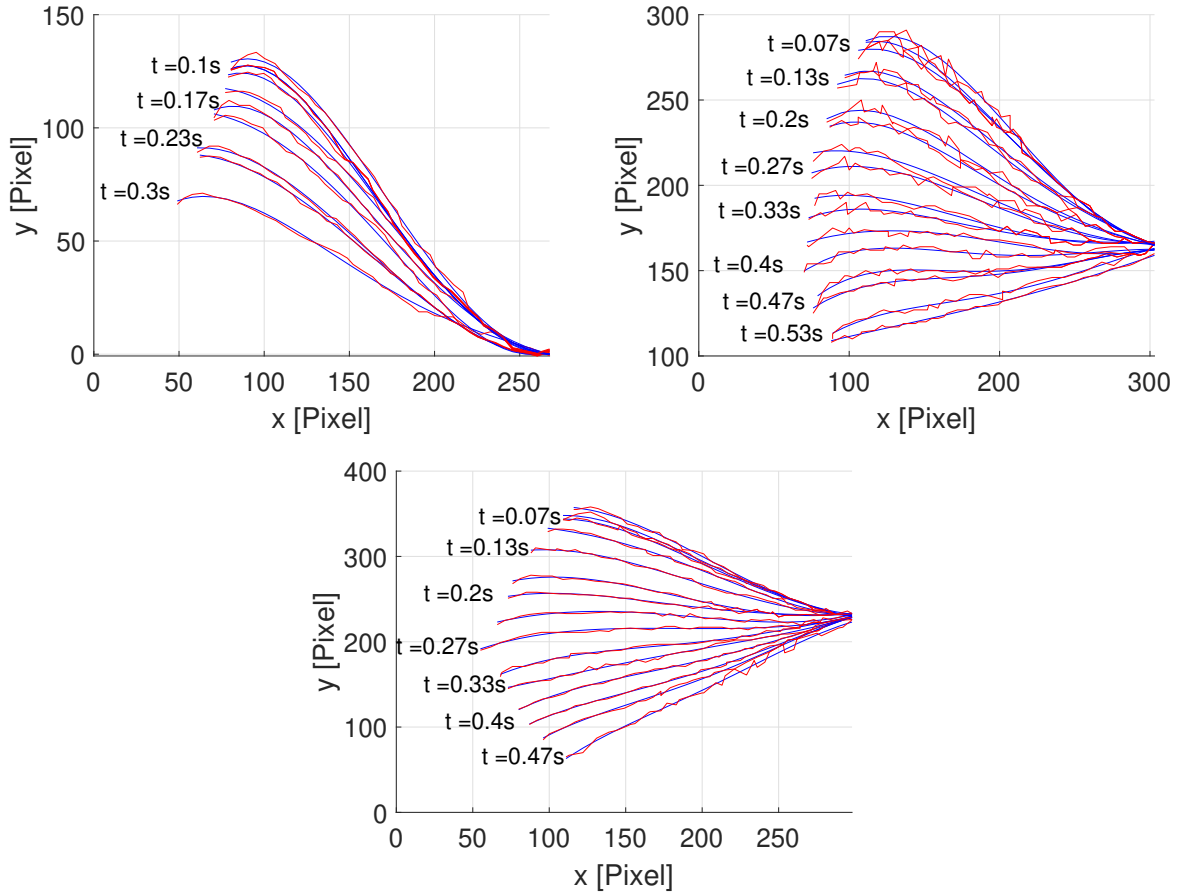


Figure 5.2: Polynomial fitting over time for three different displacements applied, described in Fig. 5.1. The red line represents the raw data manually inputted, whereas the blue line shows the product of the spatial polynomial fitting.

(RMSD) equal to 0.1547 pixels, R-square equal to 0.9946. These values were an average of the goodness of fit across all frames of the experiment shown in Fig. 5.2. For higher-order polynomial no significant improvements in the curve-fitting were observed, being that sufficient reason to use 4th order polynomial.

In addition, recalling Eq. 4.1, the drag coefficient was corrected given the proximity with a nearby boundary surface. The flagellar distance towards the boundary resulted in a drag coefficient approximately three times higher, with a value equal to 3.54×10^{-3} Pa s, given an approximate distance towards the surface equal to the smaller axis of the sperm's head ($2\mu\text{m}$).

Figure 5.2 shows the flagellar waveform relaxation given a displacement from an external magnetic field. The polynomial fitting is represented by the blue line and it is visible that accurately characterizes the flagellar distribution.

Concerning the relaxation time, experiments were done to study the impact of the displacement amplitude and the estimation of the bending stiffness, since no previous studies have statistically analysed the relation between initial displacement length and its effects on bending stiffness estimations. Hence, the null hypothesis states no difference between estimations

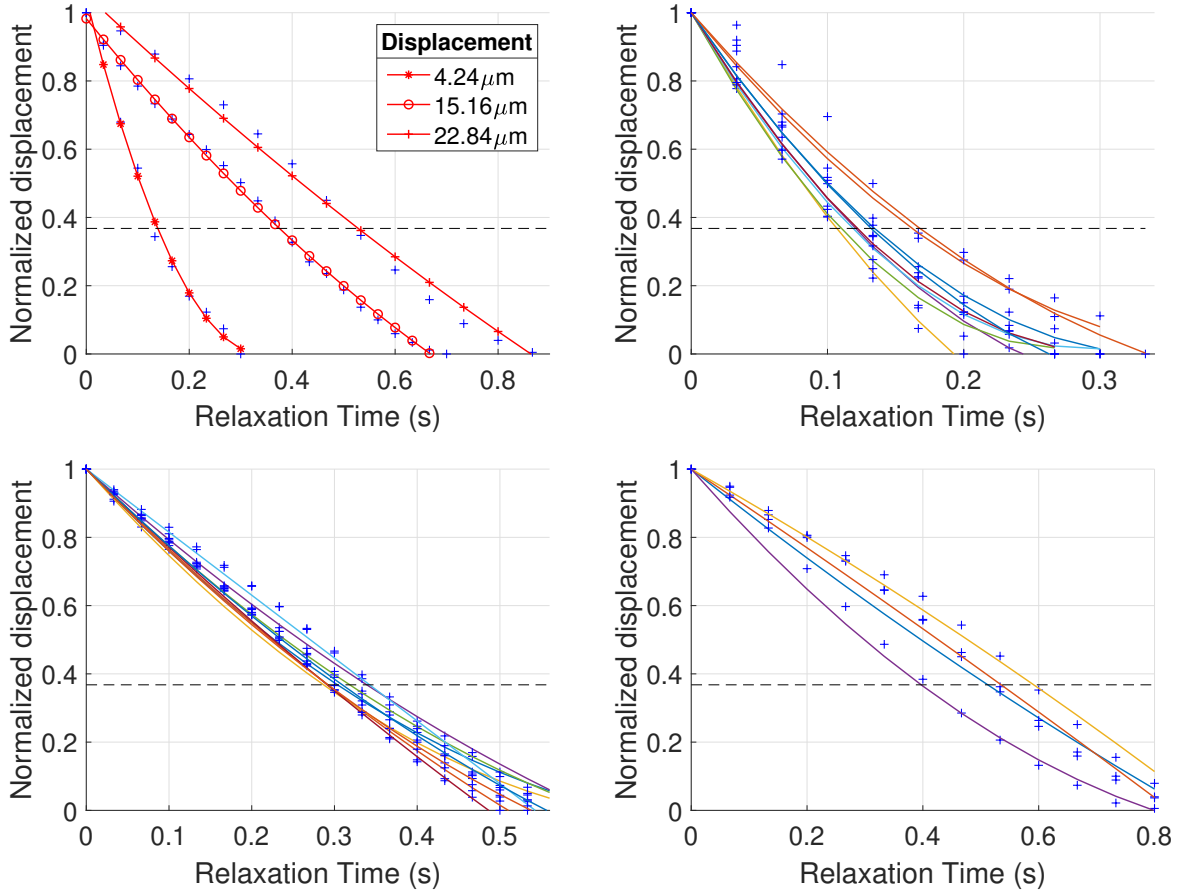


Figure 5.3: Time relaxation evolution of flagellar displacement, where the dashed grey line corresponds to $\frac{1}{e} = 0.3679$, used for the estimation of the relaxation constant τ . (a) Experimental relaxation profile for a flagellar displacement of , respectfully. (b) Experimental relaxation profile for a flagellar displacement of 4.24 μm . (c) Experimental relaxation profile for a flagellar displacement of 15.16 μm . (d) Experimental relaxation profile for a flagellar displacement of 22.84 μm .

($H_0 : IE_1 = IE_2 = IE_3$), against the alternative hypothesis ($H_1 : IE_1 \neq IE_2 \neq IE_3$). Figure 5.3a illustrates the flagellar displacement evolution towards the stable position for different initial displacements. Figure 5.3b portrays the relaxation profile given an average displacement of 4.24 μm showing that the flagellum spent approximately 0.312 ± 0.04 s to reach stability. For the wider displacements, the relaxation time was 0.627 ± 0.060 and 0.967 ± 0.039 represented in Fig. 5.3c and 5.3d, respectively.

Recalling Eq. 4.3, the natural relaxation should follow an exponential decay, where τ represents the exponential decay constant. This constant correlates with time when the decay reaches 0.3679 of the initial displacement, represented by the dashed grey line in Fig. 5.3. All experimental results showing the influence of the displacement and the estimated bending stiffness were summed up in Table 5.1.

From Table 5.1, relaxation time methodology appears to vary over different displacements applied. To compare the different metrics, we ran one-way repeated measures ANOVA tests on

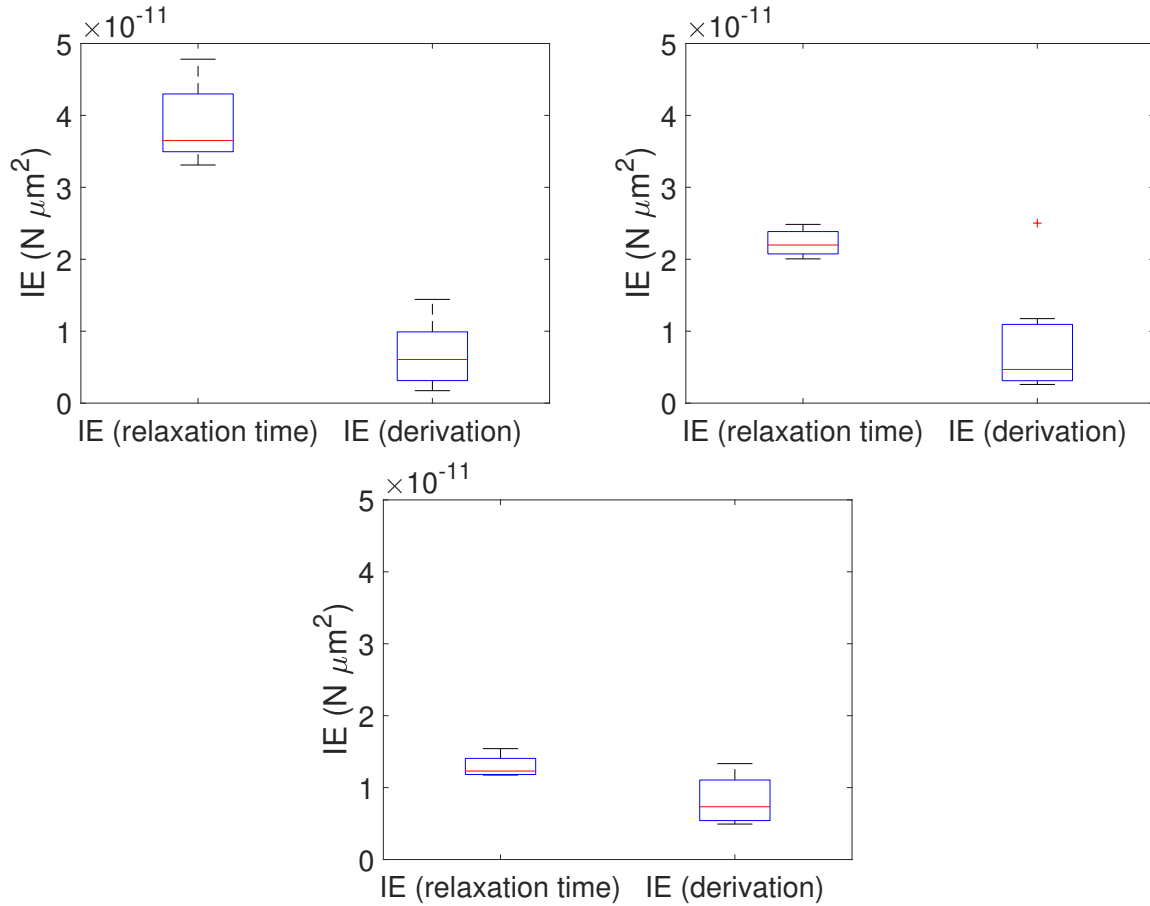


Figure 5.4: Geometric representation of the bending stiffness (IE) estimation using two methods: applying the relaxation time; direct estimation from the derivation of the equation of motion

the data ($\alpha = 0.05$). All data passed the Shapiro-Wilk normality test. Mauchly's Test of Sphericity indicated that the assumption of sphericity had been violated ($p < 0.001$). The one-way ANOVA test with a Greenhouse-Geisser correction revealed a statistically significant change between the applied displacements ($F = 1113.75$, $p < 0.001$). Thus, we reject the null hypothesis.

In theory, exponential decay characterized by the same relaxation variable (τ) should always reach half-life at, approximately, the same time independently of the initial point of decay. The same goes to our case where, independently of the initial deformation, τ should remain invariant over the different displacements. However, results in Table 5.1 disagree with those considerations. Fig 5.3 portrays different relaxation profiles compared with theoretical predictions. For higher displacements, a steeper decay should be observed after the initial release. Instead,

Table 5.1

Displacement [μm]	τ [s]	IE_r [$N\mu\text{m}^2$]	IE_d [$N\mu\text{m}^2$]
4.24 ± 0.92	0.13 ± 0.02	$2.81(\pm 0.54)10^{-10}$	$7.022(\pm 4.567)10^{-12}$
15.16 ± 0.75	0.314 ± 0.031	$1.25(\pm 0.11)10^{-10}$	$7.52(\pm 6.95)10^{-12}$
22.84 ± 0.52	0.509 ± 0.082	$7.15(\pm 0.21)10^{-11}$	$8.24(\pm 3.77)10^{-12}$

the flagellum moved steadily, resembling a linear movement. The difference between displacements may be related with the violation of theoretical approximations regarding the equation of motion. In fact, to ensure that our analysis is valid since Eq. 3.5 assumes small wave amplitude ($\frac{\sin \theta}{\theta} \approx 1$), the initial deflection angle (θ) should not be greater than 0.41 radians (23.5°), which yields ($\frac{\sin \theta}{\theta} > 0.97$). The following initial deflection angles applied in Fig 5.3 (a),(b),(c) are: 16.04° , 45.98° and 75.02° , respectively. Consequently, only the smaller displacement ($4.24 \mu\text{m}$) is in agreement with the small amplitude approximation, which corroborates with the exponential decay towards stability represented in Fig. 5.3 (b).

On the other hand, results from the direct derivation of the equation of motion pass the Shapiro-Wilk normality test. Sphericity was violated when applied the Mauchly's Test of Sphericity. The one-way ANOVA test with Greenhouse-Geisser correction showed no significant difference between estimations between initial displacements ($F= 0.22$, $p = 0.8014$). Thus, the null hypothesis cannot be rejected. However, the direct derivation is characterized by a high coefficient of variation(CV) (≈ 0.65), showing a less precise methodology when compared with the relaxation method ($CV \approx 0.19$). This may come from the dependence on different variables when compared with the relaxation method that only depends on the relaxation rate.

Subsequently, the previous statistical analysis converged to the conclusion that the best performing methodology relies on the appliance of an initial displacement angle lower than 25° using the relaxation equation. Using this methodology, several experiments were done in different sperm flagella to study the inter-variability between samples and robustness of the method. All results have been summarized in Tab. 5.2, where the flagellum full length, initial displacement angle and relaxation constant (τ) are represented. Tab. 5.2 represents experimental results of 10 different sperm cells with a total of 10 trials per sample.

Table 5.2: Bending stiffness of the IRONSperm derived from their bending shape in a magnetically actuated environment. The angular tip deflection was measured from its equilibrium shape. The relaxation constant (τ) was estimated by measuring the relaxation time when the flagellum reached 0.3679 of the initial displacement. The bending stiffness was derived from the analysis of the bending shape of each IRONSperm of a given length.

Length [μm]	Tip deflection [$^\circ$]	τ [s]	IE [$N\mu\text{m}^2$]
18.50	17.38	0.13	2.81×10^{-10}
52.65	5.00	0.469	2.60×10^{-9}
48.59	14.03	0.085	1.95×10^{-8}
53.99	6.03	0.133	1.88×10^{-8}
55.33	7.39	0.20	1.93×10^{-8}
45.57	4.22	0.137	1.08×10^{-8}
63.98	7.28	0.255	1.92×10^{-8}
46.75	39.03	0.172	7.91×10^{-9}
40.18	3.23	0.124	6.5×10^{-9}
48.86	11.38	0.213	7.68×10^{-9}

The average IE value obtained from 10 IRONSperm samples was $1.13 \times 10^{-8} \text{ N}\mu\text{m}$ with the standard deviation of $0.74 \times 10^{-8} \text{ N}\mu\text{m}$. Even though the bending stiffness impact of the magnetic particles present in IRONSperm tail has not been yet studied, a comparison with previously estimated IE for bull sperm can be used to get a sense of validation of this new methodology. Charles B. Lindemann⁵⁶ estimated a bending stiffness of impaled bull sperm equal to $29 \times 10^{-9} \text{ N}\mu\text{m}^2$ for a medium with no ATP. Those values were compared with motile sperm cells ($IE = 2.1 \times 10^{-9} \text{ N}\mu\text{m}^2$), showing that without ADP or ATP the flagella was 15 times stiffer than with motile flagella.

With comparison, the IE value obtained from the relaxation analysis is the same order of magnitude as those measured by Lindemann without ATP. However, results still reveal a stiffer flagellum when compared with motile cells. This difference on the magnitude of the measured bending stiffness may be directly related to the different material properties of the bio-hybrid *IRONSperm*. As the flagellar surface is mostly covered with magnetic iron nanoparticles, the impact of those particles in the elasticity of the flagellum is yet unknown.

However, there remain some questions for future considerations. First, the non-uniform magnetic coating of the nanoparticles effects onto the bending stiffness measurements. More precisely, the bending stiffness magnitude for all possible configurations of sperm-templated microrobots depending on the attachment of the nanoparticles across all the 4 segments of the sperm cell. Second, the IE corrected for taper and its influence on the swimming waveform is a required step for a better understanding of the mechanics of these microrobots. Since the used equation of motion applies to an untapered rod, stiffness values obtained from this equation must be corrected to take the taper into account.

6 CONCLUSIONS

We have investigated the bending stiffness estimation of IRONSperm which involves a very unique way of generating force and applying flagellar displacement. This novel approach is worth studying because it features a wireless process where no physical contact is needed to perform measurements.

In addition, we present a microscopic investigation on a bending stiffness estimation mechanisms using oscillating weak magnetic fields. This investigation includes the characterization of the bending stiffness using a wireless methodology of the self-assembled IRONSperm flagella. The current study shows an average bending stiffness values of $1.13 \times 10^{-8} \text{ N } \mu\text{m}$ and standard deviation of $0.74 \times 10^{-8} \text{ N } \mu\text{m}$.

The current results seem to be a plausible alternative to the current direct methodology to estimate the bending stiffness. The fabrication process is relatively flexible and enables the production of robotic sperms with similar morphology to that of sperm cells. Furthermore, head adherence to the glass container appears to be a recurrent phenomenon, allowing a methodology repeatable and consistent to find via microscopic imaging.

REFERENCES

- ¹ P Fischer and S Palagi. Bioinspired microrobots. *Nat. Rev. Mater*, 3:113–124, 2018.
- ² Jinxing Li, Berta Esteban-Fernández de Ávila, Wei Gao, Liangfang Zhang, and Joseph Wang. Micro/nanorobots for biomedicine: Delivery, surgery, sensing, and detoxification. *Science Robotics*, 2(4), 2017.
- ³ Wei Wang, Luz Angelica Castro, Mauricio Hoyos, and Thomas E Mallouk. Autonomous motion of metallic microrods propelled by ultrasound. *ACS nano*, 6(7):6122–6132, 2012.
- ⁴ Xiang-Zhong Chen, Bumjin Jang, Daniel Ahmed, Chengzhi Hu, Carmela De Marco, Marcus Hoop, Fajer Mushtaq, Bradley J Nelson, and Salvador Pané. Small-scale machines driven by external power sources. *Advanced Materials*, 30(15):1705061, 2018.
- ⁵ Feng Guo, Peng Li, Jarrod B French, Zhangming Mao, Hong Zhao, Sixing Li, Nitesh Nama, James R Fick, Stephen J Benkovic, and Tony Jun Huang. Controlling cell–cell interactions using surface acoustic waves. *Proceedings of the National Academy of Sciences*, 112(1):43–48, 2015.
- ⁶ Jianhe Guo, Jeremie June Gallegos, Ashley Robyn Tom, and Donglei Fan. Electric-field-guided precision manipulation of catalytic nanomotors for cargo delivery and powering nano-electromechanical devices. *ACS nano*, 12(2):1179–1187, 2018.
- ⁷ Islam SM Khalil, Ahmet Fatih Tabak, Anke Klingner, and Metin Sitti. Magnetic propulsion of robotic sperms at low-reynolds number. *Applied Physics Letters*, 109(3):033701, 2016.
- ⁸ Islam SM Khalil, Alaa Adel, Dalia Mahdy, Mina M Micheal, Mohanad Mansour, Nabila Hamdi, and Sarthak Misra. Magnetic localization and control of helical robots for clearing superficial blood clots. *APL bioengineering*, 3(2):026104, 2019.
- ⁹ Islam SM Khalil, Herman C Dijkslag, Leon Abelmann, and Sarthak Misra. Magnetosperm: A microrobot that navigates using weak magnetic fields. *Applied Physics Letters*, 104(22):223701, 2014.
- ¹⁰ Islam SM Khalil, Ahmet Fatih Tabak, Youssef Hamed, Mohamed E Mitwally, Mohamed Tawakol, Anke Klingner, and Metin Sitti. Swimming back and forth using planar flagellar propulsion at low reynolds numbers. *Advanced Science*, 5(2):1700461, 2018.

- ¹¹ On Shun Pak, Wei Gao, Joseph Wang, and Eric Lauga. High-speed propulsion of flexible nanowire motors: Theory and experiments. *Soft Matter*, 7(18):8169–8181, 2011.
- ¹² Stefan Klumpp and Damien Faivre. Magnetotactic bacteria. *The European Physical Journal Special Topics*, 225(11-12):2173–2188, 2016.
- ¹³ Islam SM Khalil, Veronika Magdanz, Juliane Simmchen, Anke Klingner, and Sarthak Misra. Resemblance between motile and magnetically actuated sperm cells. *Applied Physics Letters*, 116(6):063702, 2020.
- ¹⁴ Michael P Kummer, Jake J Abbott, Bradley E Kratochvil, Ruedi Borer, Ali Sengul, and Bradley J Nelson. Octomag: An electromagnetic system for 5-dof wireless micromanipulation. *IEEE Transactions on Robotics*, 26(6):1006–1017, 2010.
- ¹⁵ Rémi Dreyfus, Jean Baudry, Marcus L Roper, Marc Fermigier, Howard A Stone, and Jérôme Bibette. Microscopic artificial swimmers. *Nature*, 437(7060):862–865, 2005.
- ¹⁶ Shuxiang Guo, Jun Sawamoto, and Qingxue Pan. A novel type of microrobot for biomedical application. In *2005 IEEE/RSJ International Conference on Intelligent Robots and Systems*, pages 1047–1052. IEEE, 2005.
- ¹⁷ Shuxiang Guo, Qinxue Pan, and Mir Behrad Khamesee. Development of a novel type of microrobot for biomedical application. *Microsystem Technologies*, 14(3):307–314, 2008.
- ¹⁸ Ali Ghanbari, Mohsen Bahrami, and Mohammad RH Nobari. Methodology for artificial microswimming using magnetic actuation. *Physical Review E*, 83(4):046301, 2011.
- ¹⁹ Sylvain Martel, Charles C Tremblay, Serge Ngakeng, and Guillaume Langlois. Controlled manipulation and actuation of micro-objects with magnetotactic bacteria. *Applied Physics Letters*, 89(23):233904, 2006.
- ²⁰ Dominic De Lanauze, Ouajdi Felfoul, Jean-Philippe Turcot, Mahmood Mohammadi, and Sylvain Martel. Three-dimensional remote aggregation and steering of magnetotactic bacteria microrobots for drug delivery applications. *The International Journal of Robotics Research*, 33(3):359–374, 2014.
- ²¹ Jason J Benkoski, Jennifer L Breidenich, O Manuel Uy, Allen T Hayes, Ryan M Deacon, H Bruce Land, Jane M Spicer, Pei Yui Keng, and Jeffrey Pyun. Dipolar organization and magnetic actuation of flagella-like nanoparticle assemblies. *Journal of Materials Chemistry*, 21(20):7314–7325, 2011.
- ²² Henning Pedersen. Observations on the axial filament complex of the human spermatozoon. *Journal of ultrastructure research*, 33(5-6):451–462, 1970.
- ²³ IR Gibbons. Chemical dissection of cilia. *Archives de biologie*, 76(2):317–352, 1965.
- ²⁴ RW Linck. Advances in the ultrastructural analysis of the sperm flagellar axoneme. *The spermatozoon*, pages 99–115, 1979.

- ²⁵ CJ Brokaw. Elastase digestion of demembrated sperm flagella. *Science*, 207(4437):1365–1367, 1980.
- ²⁶ B Baccetti, V Pallini, and AG Burrini. Structure and chemical composition of the bull sperm” coarse fibers.”. *J. submicrosc. Cytol*, 5:237–256, 1973.
- ²⁷ MR Curry and PF Watson. Sperm structure and function. dalam: Grudzinskas jg and yovich jl eds. gametes-the spermatozoon, 1995.
- ²⁸ Richard Oko. Comparative analysis of proteins from the fibrous sheath and outer dense fibers of rat spermatozoa. *Biology of reproduction*, 39(1):169–182, 1988.
- ²⁹ DM Woolley and SN Nickels. Microtubule termination patterns in mammalian sperm flagella. *Journal of ultrastructure research*, 90(3):221–234, 1985.
- ³⁰ Don W Fawcett. The anatomy of the mammalian spermatozoon with particular reference to the guinea pig. *Zeitschrift für Zellforschung und Mikroskopische Anatomie*, 67(3):279–296, 1965.
- ³¹ James Gray. Croonian lecture—aspects of animal locomotion. *Proceedings of the Royal Society of London. Series B-Biological Sciences*, 128(850):28–62, 1939.
- ³² J Gray. Undulatory propulsion. *Journal of Cell Science*, 3(28):551–578, 1953.
- ³³ James Gray and GJ Hancock. The propulsion of sea-urchin spermatozoa. *Journal of Experimental Biology*, 32(4):802–814, 1955.
- ³⁴ Robert Rikmenspoel. Elastic properties of the sea urchin sperm flagellum. *Biophysical journal*, 6(4):471–479, 1966.
- ³⁵ Robert Rikmenspoel. The tail movement of bull spermatozoa: observations and model calculations. *Biophysical journal*, 5(4):365–392, 1965.
- ³⁶ Veronika Magdanz, Islam SM Khalil, Juliane Simmchen, Guilherme P Furtado, Sumit Mohanty, Johannes Gebauer, Haifeng Xu, Anke Klingner, Azaam Aziz, Mariana Medina-Sánchez, et al. Ironsperm: Sperm-templated soft magnetic microrobots. *Science Advances*, 6(28):eaba5855, 2020.
- ³⁷ Veronika Magdanz, Johannes Gebauer, Priyanka Sharan, Samar Eltoukhy, Dagmar Voigt, and Juliane Simmchen. Sperm–particle interactions and their prospects for charge mapping. *Advanced Biosystems*, 3(9):1900061, 2019.
- ³⁸ M Beleggia, M De Graef, and YT Millev. The equivalent ellipsoid of a magnetized body. *Journal of Physics D: Applied Physics*, 39(5):891, 2006.
- ³⁹ Jack William Judy. *Batch-fabricated ferromagnetic microactuators with silicon flexures*. PhD thesis, University of California, Berkeley, 1996.
- ⁴⁰ Jake J Abbott, Olgaç Ergeneman, Michael P Kummer, Ann M Hirt, and Bradley J Nelson. Modeling magnetic torque and force for controlled manipulation of soft-magnetic bodies. *IEEE Transactions on Robotics*, 23(6):1247–1252, 2007.

- ⁴¹ Philip McCord Morse, Acoustical Society of America, and American Institute of Physics. *Vibration and sound*, volume 2. McGraw-Hill New York, 1948.
- ⁴² KE Machin. Wave propagation along flagella. *Journal of Experimental Biology*, 35(4):796–806, 1958.
- ⁴³ Robert Rikmenspoel. Contractile mechanisms in flagella. *Biophysical journal*, 11(5):446–463, 1971.
- ⁴⁴ CK Omoto and CJ Brokaw. Structure and behaviour of the sperm terminal filament. *Journal of cell science*, 58(1):385–409, 1982.
- ⁴⁵ Robert Rikmenspoel and Michael A Sleight. Bending moments and elastic constants in cilia. *Journal of Theoretical Biology*, 28(1):81–100, 1970.
- ⁴⁶ Norman Derby and Stanislaw Olbert. Cylindrical magnets and ideal solenoids. *American Journal of Physics*, 78(3):229–235, 2010.
- ⁴⁷ DM Woolley. Motility of spermatozoa at surfaces. *REPRODUCTION-CAMBRIDGE-*, 126(2):259–270, 2003.
- ⁴⁸ Benjamin M Friedrich, Ingmar H Riedel-Kruse, Jonathon Howard, and Frank Jülicher. High-precision tracking of sperm swimming fine structure provides strong test of resistive force theory. *Journal of Experimental Biology*, 213(8):1226–1234, 2010.
- ⁴⁹ Jonathan Ferracci. *Hydrodynamics of ciliates at the air-liquid interface*. PhD thesis, Tohoku University, 2013.
- ⁵⁰ David J Smith, EA Gaffney, H Gadêlha, N Kapur, and JC Kirkman-Brown. Bend propagation in the flagella of migrating human sperm, and its modulation by viscosity. *Cell motility and the cytoskeleton*, 66(4):220–236, 2009.
- ⁵¹ Toru Hyakutake, Koichi Sato, and Kenta Sugita. Study of bovine sperm motility in shear-thinning viscoelastic fluids. *Journal of biomechanics*, 88:130–137, 2019.
- ⁵² Christopher Brennen and Howard Winet. Fluid mechanics of propulsion by cilia and flagella. *Annual Review of Fluid Mechanics*, 9(1):339–398, 1977.
- ⁵³ CURTIS G GRAVANCE, R Vishwanath, COLIN PITT, DUANE L GARNER, and PATRICK J CASEY. Effects of cryopreservation on bull sperm head morphometry. *Journal of andrology*, 19(6):704–709, 1998.
- ⁵⁴ Kathleen A Lesich, Dominic W Pelle, and Charles B Lindemann. Insights into the mechanism of adp action on flagellar motility derived from studies on bull sperm. *Biophysical journal*, 95(1):472–482, 2008.
- ⁵⁵ Kathleen A Schmitz-Lesich and Charles B Lindemann. Direct measurement of the passive stiffness of rat sperm and implications to the mechanism of the calcium response. *Cell motility and the cytoskeleton*, 59(3):169–179, 2004.

⁵⁶ Charles B Lindemann, Walter G Rudd, and Robert Rikmenspoel. The stiffness of the flagella of impaled bull sperm. *Biophysical journal*, 13(5):437–448, 1973.